NUCL SCI TECH (2021) 32:57
https://doi.org/10.1007/s41365-021-00893-z

In situ studies on the positive and negative effects of 1,8-diiodoctane on the device performance and morphology evolution of organic solar cells

Da Huang[1,2,4] · **Chun-Xia Hong**[1,2] · **Jian-Hua Han**[3,5] · **Nie Zhao**[6] · **Xiu-Hong Li**[1,2,4] · **Xi-Chang Bao**[3,5] · **Feng-Gang Bian**[1,2,4] · **Yu-Ying Huang**[1,2,4] · **Chun-Ming Yang**[1,2,4]

Received: 11 February 2021 / Revised: 16 April 2021 / Accepted: 19 April 2021 / Published online: 9 June 2021

Abstract The introduction of solvent additives is one of the most common approaches for enhancing the power conversion efficiency of organic solar cells (OSCs). However, the use of solvent additives has some negative effects, and an understanding of how solvent additives affect OSCs is currently limited. In this study, we developed an in situ grazing incidence wide-angle X-ray scattering (GIWAXS) technique in the SAXS beamline (BL16B1) at the Shanghai Synchrotron Radiation Facility, and the additive effects of 1,8-diiodoctane (DIO) on the performance and morphology evolution of the PTB7-Th/PC$_{71}$BM device was investigated in depth. The results revealed that the crystal size increased with the volume ratio of DIO, and a drastic evolution of lattice space and crystal coherence length was observed during thermal annealing for the first time, to our knowledge. The discrete PC$_{71}$BM molecules dissolved by DIO have an effect similar to that of the nucleating agent for PTB7-Th, boosting the crystallization of PTB7-Th, reducing phase separation, and inducing more drastic morphological evolution during thermal annealing. Our results provide a deep perspective for the mechanism of solvent additives, while also showing the significance and feasibility of the in situ GIWAXS technique we developed at BL16B1.

Keywords Grazing incidence wide-angle X-ray scattering · Grazing incidence small-angle X-ray scattering · Organic solar cells · Solvent additive · Thermal stability

1 Introduction

Organic solar cells (OSCs), which are lightweight, flexible, and environmentally friendly [1], have power conversion efficiencies (PCEs) of over 17.5% [2]. The morphology of the active layer plays a crucial role in the performance of OSCs [3], which can be manipulated by several approaches, such as the selection of donor and acceptor materials [4], selection of the used solvent [5], thermal annealing [6], solvent vapor annealing [7], upside down solvent annealing treatment [8], and the addition of

---

This work was supported by the National Natural Science Foundation of China (Nos. U1932118, 2005324) and the National Key R&D Program of China (Nos. 2017YFA0403002, 2018YFB0704201).

Supplementary Information The online version contains supplementary material available at https://doi.org/10.1007/s41365-021-00893-z.

✉ Yu-Ying Huang
huangyuying@zjlab.org.cn

✉ Chun-Ming Yang
yangchunming@zjlab.org.cn

[1] Shanghai Synchrotron Radiation Facility, Shanghai Institute of Applied Physics, Chinese Academy of Sciences, Shanghai 201204, China

[2] Shanghai Advanced Research Institute, Chinese Academy of Sciences, Shanghai 201210, China

[3] CAS Key Laboratory of Bio-Based Materials, Qingdao Institute of Bioenergy and Bioprocess Technology, Chinese Academy of Sciences, Qingdao 266101, China

[4] University of Chinese Academy of Sciences, Beijing 100049, China

[5] Functional Laboratory of Solar Energy, Shandong Energy Institute, Qingdao 266101, China

[6] College of Materials Science and Engineering, Xiangtan University, Xiangtan 411105, China

solvent additives [9]. For the solvent additive approach, 1,8-diiodoctane (DIO) is one of the most commonly used solvent additives to enhance OSC device performance [10]. However, a series of negative effects, such as light instability, thermal instability, and long-term instability, can be induced by the use of DIO [11]. However, the mechanism of both the positive and negative effects of DIO usage on morphology is not yet completely understood. Grazing incidence wide-angle X-ray scattering (GIWAXS), which provides statistical information in a large region, is sensitive to the surface and inner structure information of the active layer [12]. More importantly, in situ GIWAXS can monitor the dynamic evolution of active layer morphology, which is of great importance for related mechanism research [13]. Most of the current research was based on ex situ GIWAXS methods to characterize the active layer morphology [14], and therefore, the understanding of the mechanism remains limited. In this study, we developed an in situ GIWAXS technique in the small-angle X-ray scattering beamline (BL16B1) at the Shanghai Synchrotron Radiation Facility (SSRF) and probed the dynamic morphology evolution of the active layer of a typical fullerene system of OSCs with donor poly[(ethylhexyl-thiophenyl)-benzodithiophene-(ethylhexyl)-thienothiophene] (PTB7-Th) and acceptor [6,6]-phenyl C_{71}-butyric acid methyl ester ($PC_{71}BM$). A phenomenon in which the evolution was enlarged with an increase in the proportion of DIO being observed for the first time. The mechanism by which the discrete $PC_{71}BM$ molecules dissolved by DIO had a similar effect to that of the nucleating agent for PTB7-Th, leading to a larger crystal size of PTB7-Th, thereby, promoting the morphology evolution during thermal annealing, was revealed, and is of great significance for the further development of OSCs.

2 Experimental section

2.1 Development of the in situ GIWAXS technique

The small-angle X-ray scattering (SAXS) beamline (BL16B1) at the SSRF [15], which mainly engages in the application of X-ray scattering [16], provides perfect conditions for the development of the GIWAXS method. Figure 1 shows the developed GIWAXS setup for BL16B1. PILATUS3 X 2 M was employed as a 2D area detector, and the pixel size was 172 µm × 172 µm, the number of pixels was 1475 × 1679, and the maximum frame rate was 250 Hz. The high frame rate guaranteed the ability to collect data during time-resolved measurements. The incident angle could be adjusted by the sample stage, which comprised four Kohzu stages, from 0° to 2°. The four Kohzu stages control the height and shift in the *YZ* plane, rotation on the *y*-axis, and rotation on the *x*-axis. The glove box, as shown in Fig. 1, provided a gaseous atmosphere for the samples and reduced background scattering. The sample temperature was controlled with a homemade temperature controller using a thermocouple that was thermally connected to the top of the sample stage. The temperature range was 25–200 °C.

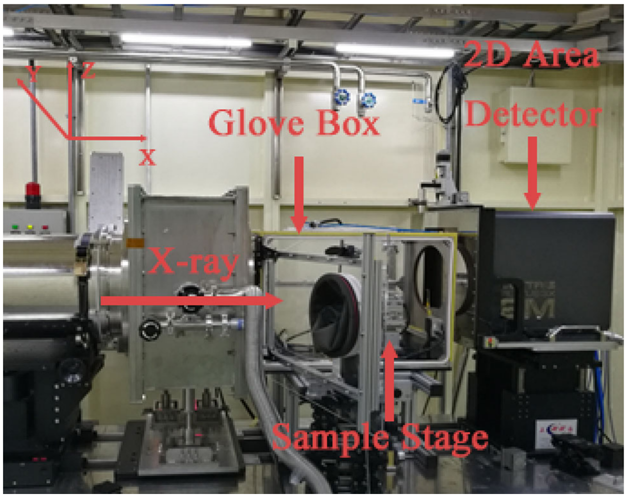

Fig. 1 (Color online) Photograph of grazing incidence wide-angle X-ray scattering setup at BL16B1

2.2 GIWAXS and GISAXS measurements

For GIWAXS and GISAXS measurements, samples were fabricated by spin-coating the respective solutions of active layers onto 1.5 × 1.5 cm^2 silicon substrates with pre-coated PEDOT: PSS (30 nm). Silicon substrates were cleaned in sequence with detergent; deionized water; acetone; and isopropyl alcohol in an ultrasonic bath for 15 min, dried by ultra-pure N_2, and then treated with O_2 plasma for 8 min. The GIWAXS and GISAXS measurements were carried out using beamline BL16B1 at the SSRF. The beam size was 0.4 × 0.5 mm^2, and the photon flux at the sample was 1×10^{11} phs/s. The X-ray wavelength was 0.124 nm ($E = 10$ keV), and the incident angle was set at 0.15°, which was close to the critical angle, to maximize the intensity. The sample-to-detector distance was 266.2 and 1997.6 mm for GIWAXS and GISAXS measurements, respectively, which was calibrated with the standard sample of silver behenate. For the static measurements, the exposure time of individual measurements was 60 s. For in situ measurements, samples were heated with a hotplate under an air atmosphere. Single images were collected every 60 s to obtain a high signal-to-noise ratio and high sampling rate. For each set of experiments, the pixel coordinates of the images were converted into q values after correction of the beam center by standard samples. One-dimensional profiles in the out-of-plane direction were obtained by integrating at the azimuthal angle around 90°, while the profiles in the in-plane direction were extracted with an azimuthal angle of approximately 0°.

2.3 Materials

All reagents and solvents were obtained from commercial sources and used directly without further purification. *N*, *N*-Dioxide of bis(*N*,*N*′-dimethylaminopropyl)perylene diimide (PDINO) was purchased from Solarmer Materials Inc. (Beijing, China). Poly(3,4 ethylenedioxythiophene):poly(styrenesulfonate) (PEDOT:PSS) (PH1000) was obtained from Heraeus Inc. PTB7-Th was purchased from One-Material Corp. The $PC_{71}BM$, chlorobenzene, and 1,8-diiodooctane (DIO) used in the device fabrication processes were obtained from Sigma-Aldrich.

2.4 Device fabrication

The OSC devices were fabricated with the configuration ITO/PEDOT:PSS/active layer/PDINO/Al. ITO substrates were cleaned with detergent, deionized water, acetone, and isopropyl alcohol in an ultrasonic bath sequentially for 15 min, then dried by ultra-pure N_2, and finally treated with O_2 plasma for 8 min. Then, a 30 nm PEDOT:PSS layer was spin-coated onto the ITO-coated glass at 4,000 rpm and baked at 150 °C for 20 min in an oven. The PTB7-Th/$PC_{71}BM$ solution was prepared by dissolving blends with a weight ratio of 1:1.5 in chlorobenzene (total concentration 20 mg/mL, with 0, 1, 3, and 8 vol% DIO additive). When the substrates were transferred into a glove box, the solutions were stirred overnight and spin-coated on the PEDOT: PSS layer to form active layers (the optimal thickness was approximately 100 nm). Subsequently, a PDINO solution (in CH_3OH, 1 mg/mL) was spin-coated at 3,000 rpm for 15 s to form the electron transfer layer. Finally, the Al (100 nm) metal electrode was thermally evaporated under approximately 4×10^{-4} Pa, and the device area was 0.1 cm^2, defined by a shadow mask.

2.5 Annealing process

To perform in situ investigations on device PCE and active layer morphology, an annealing strategy that involved placing devices on the hot plate at room temperature (25 °C) and then heating them to the annealing temperature (100 °C) at a heating rate of 20 °C/min was employed to simulate the conventional thermal annealing strategy that involved directly placing devices on a hot plate that had been heated to a specified temperature. Hence, it would remain for 3.75 min in the heating stage process from 25 °C to 100 °C, 10 min in the temperature holding process at 100 °C, and 3.75 min in the cooling process from 100 °C to 25 °C.

3 Results and discussion

3.1 DIO addition effects on device PCE and thermal stability

To demonstrate the effects of using DIO on the PTB7-Th/$PC_{71}BM$ device, devices with various ratios of DIO ranging from 0 to 8 vol% were fabricated with a conventional device structure of ITO/PEDOT:PSS/active layer/PDINO/Al, as shown in Fig. 2. The *J*–*V* curves are shown in Fig. 3a, and the detailed photovoltaic parameters for devices with various ratios of added DIO are shown in Fig. 3b and Table 1. As shown in Fig. 3a, a drastic change in the *J*–*V* curve of the PTB7-Th/$PC_{71}BM$ device was induced by the addition of DIO. The *J*–*V* curve for the device without DIO showed an unfavorable shape with a low short-circuit current density (J_{SC}) and fill factor (FF) compared with the values for devices with added DIO.

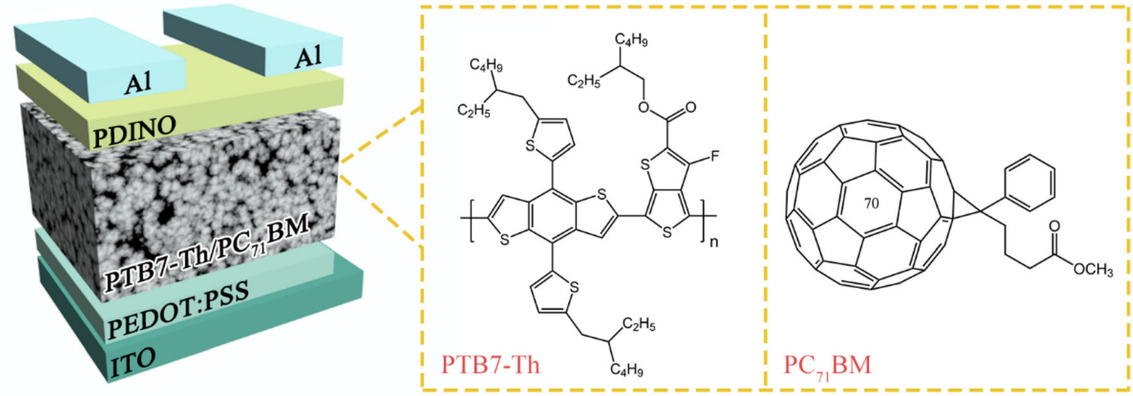

Fig. 2 (Color online) Device configuration and the molecular structures of PTB7-Th and $PC_{71}BM$

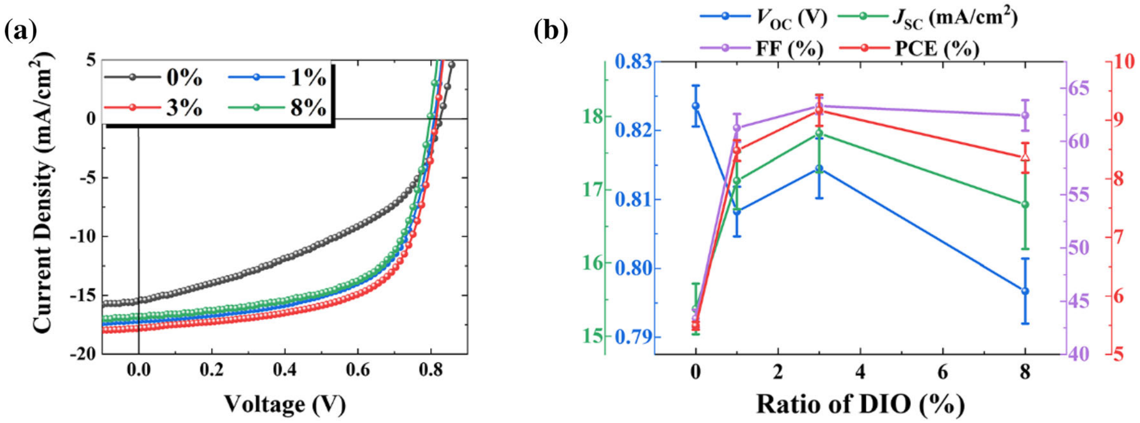

Fig. 3 (Color online) **a** *J*–*V* curves and **b** photovoltaic parameters of organic solar cell devices based on PTB7-Th/PC$_{71}$BM devices with various ratios of 1,8-diiodoctane ranging from 0 to 8 vol%. The average parameters were calculated from 20 independent devices. DIO, 1,8-diiodoctane; V_{OC}, open circuit voltage; J_{SC}, low short-circuit current density; FF, fill factor; PCE, power conversion efficiency

Table 1 Photovoltaic parameters of PTB7-Th/PC$_{71}$BM devices with various ratios of 1,8-diiodoctane

Ratio of DIO	V_{OC} (V)	J_{SC} (mA/cm^2)	FF (%)	PCE (%)
0 v%	0.82 (± 0.00)	15.37 (± 0.35)	43.37 (± 0.83)	5.49 (± 0.07)
1 v%	0.81 (± 0.00)	17.13 (± 0.39)	61.27 (± 1.31)	8.48 (± 0.18)
3 v%	0.82 (± 0.00)	17.77 (± 0.53)	63.33 (± 0.76)	9.17 (± 0.27)
8 v%	0.80 (± 0.01)	16.80 (± 0.61)	62.45 (± 1.44)	8.36 (± 0.25)

The average parameters were calculated from more than 20 independent devices. DIO, 1,8-diiodoctane; V_{OC}, open circuit voltage; J_{SC}, low short-circuit current density; FF, fill factor; PCE, power conversion efficiency

While the values of open circuit voltage (V_{OC}) for the device without the addition of DIO were basically the same as the value for devices with different ratios of DIO, a trend of decreasing with the increase in DIO was observed. As shown in Fig. 3b, the PCE was only 5.49% when no DIO was added. As the ratio of DIO increased, the value of PCE first increased to 8.48% for the device with 1 vol% DIO, and a maximum value of 9.17% was achieved for devices with 3 vol% DIO. However, the PCE value decreased to 8.36% when the DIO ratio increased to 8 vol%. These results demonstrate that the appropriate addition of DIO can improve the PCE of PTB7-Th/PC$_{71}$BM devices, while the excessive addition of DIO could harm the device performance. A similar phenomenon in PTB7/PC$_{71}$BM was reported by Kim et al. [17].

As shown in Fig. 3b, for devices with no added DIO, the values of V_{OC}, J_{SC}, and FF were 0.83 V, 15.37 mA/cm^2, and 43.37%, respectively. After adding DIO, the value of V_{OC} showed a trend of decreasing with an increase in DIO proportion, where the median value of 0.82 V was obtained from the device with 3 vol% DIO added. For J_{SC} and FF, the values significantly increased after the addition of DIO, and maximum values of 17.77 mA/cm^2 and 63.33% were achieved, respectively, when the ratio of DIO was 3 vol%, leading to the optimum PCE. However, when the ratio of DIO was increased to 8 vol%, both the FF and J_{SC} values decreased, resulting in a decrease in PCE. The increase in J_{SC} and FF appeared to be the main reason for the improvement in PCE induced by the addition of DIO. For OSCs, V_{OC} is generally influenced by the morphology of the active layer, especially large-scale phase separation [18]. J_{SC} and FF are usually dominated by the generation, diffusion, and dissociation of photogenerated excitons and the transport and collection of charge, which are strongly dependent on the donor/acceptor interface and charge transport channel in the active layer [19]. Therefore, the photovoltaic parameters changed with various ratios of DIO, suggesting that there was a morphological evolution in the active layer.

Typical PTB7-Th/PC$_{71}$BM devices suffer severe PCE degradation even after short-term thermal annealing at temperatures ranging from 70 to 150 °C [20]. The addition of DIO can further harm the thermal stability of OSC devices [21]. However, the mechanism by which DIO can harm the thermal stability of PTB7-Th/PC$_{71}$BM devices is not yet completely understood. Figure 4a, b show the *J*–*V* curves and normalized photovoltaic parameters obtained after 10 min of thermal annealing at 100 °C for PTB7-Th/

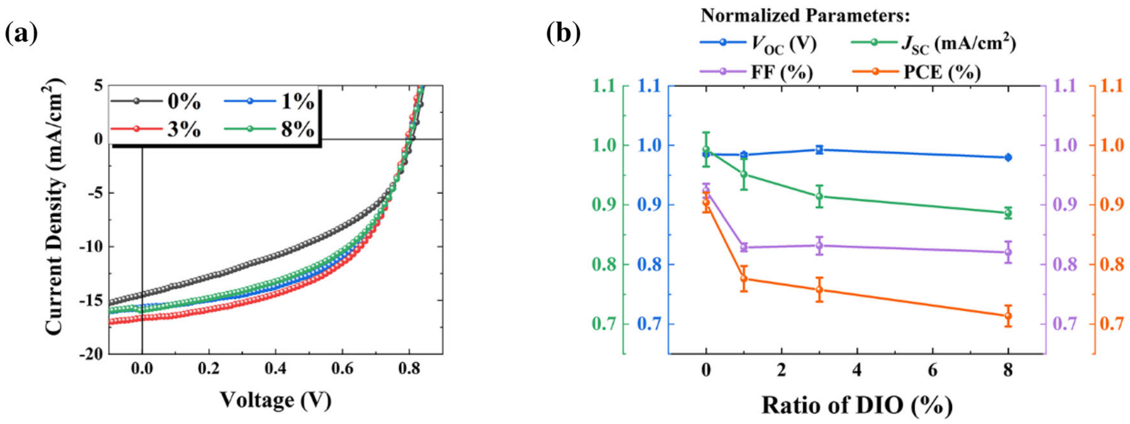

Fig.4 (Color online) **a** *J*–*V* curves and **b** normalized photovoltaic parameters of organic solar cell devices based on PTB7-Th/PC$_{71}$BM devices with various ratios of 1,8-diiodoctane ranging from 0 to 8 vol% after 10 min of thermal annealing at 100 °C. The average parameters were calculated from 20 independent devices. DIO, 1,8-diiodoctane; V_{OC}, open circuit voltage; J_{SC}, low short-circuit current density; FF, fill factor; PCE, power conversion efficiency

PC$_{71}$BM blends with various ratios of added DIO. As shown in Fig. 4a, the *J*–*V* curve after thermal annealing for the device without DIO showed an insignificant change compared to that of the *J*–*V* curve before annealing (Fig. 3a). However, drastic changes were observed for devices with various proportions of DIO, where the changes were primarily induced by the decrease in J_{SC} and FF. As shown in Fig. 4b, after thermal annealing, the residual J_{SC}, FF, and PCE values were 99.3%, 92.4%, and 90.4%, respectively, of their initial values for devices without DIO. However, only 95.1%, 82.9%, and 77.6% of J_{SC}, FF, and PCE, respectively, were retained for the devices with 1 vol% DIO. For devices with 3 vol% DIO, the J_{SC}, FF, and PCE values were 91.4%, 83.2%, and 75.8%, respectively. When the proportion of DIO was further increased to 8 vol%, the residual J_{SC}, FF, and PCE values decreased to 88.7%, 82.1%, and 71.4%, respectively. The degradation in J_{SC}, FF, and PCE increased after the addition of DIO. In addition, these three parameters showed a decreasing trend as the proportion of DIO increased. However, the value of residual V_{OC} was approximately unchanged with the increase in DIO, which demonstrated that the effect of DIO on V_{OC} could be negligible and no large-scale phase separation was induced during thermal annealing. The photovoltaic parameters after thermal annealing are summarized in Table S1. These results demonstrate the negative effect of DIO addition on the thermal stability of the PTB7-Th/PC$_{71}$BM devices.

3.2 Effects of addition of DIO on the morphology of the active layer to improve device performance

To further explore the mechanism by which addition of various ratios of DIO improves device performance, GIWAXS measurements were carried out to monitor the evolution of the active layer morphology after adding various ratios of DIO. The 2D GIWAXS patterns of the blends with various ratios of DIO are shown in Fig. S1. Figure 5a, b show the 1D profiles integrated from the 2D patterns in the out-of-plane and in-plane directions, respectively. For the typical PTB7-Th/PC$_{71}$BM blends with 3 vol% DIO, the polymer alkyl stacking peaks showed an almost ring-like scattering pattern at $q \approx 2.90$ nm^{-1} with an associated lattice spacing of $d \approx 2.17$ nm, which corresponds to the (100) Bragg reflection and is consistent with that of previous results [22]. The almost ring-like scattering pattern of PC$_{71}$BM was observed at $q \approx 13.60$ nm^{-1}, which demonstrated that the PC$_{71}$BM molecules were in an amorphous state. A weak π–π stacking peak, which could hardly be distinguished from the ring of PC$_{71}$BM, occurred in the out-of-plane direction, implying that the PTB7-Th lamellae had a preference for face-on orientation. The lamellar structure was likely to form nanofibrils under common processing conditions, which could be inclined relative to the substrate, causing the peaks to have an angle spread in the scattering patterns.

For the (100) peak of PTB7-Th shown in Fig. 5a, b, a weak peak occurred in the blend film without DIO owing to the poor crystallinity of PTB7-Th [22]. The peak intensity increased with decreasing peak width in both the out-of-plane and in-plane directions as the ratio of DIO increased. These results suggested that the crystallization of PTB7-Th could be enhanced by increasing the proportion of DIO. The changes in the peak position and full width at half maximum (FWHM) were also observed after adding various proportions of DIO, indicating that DIO could influence the lattice space (*d*-spacing) and crystal coherence length (CCL) of PTB7-Th. For the peak of PC$_{71}$BM, slight changes in FWHM were also observed for blends with

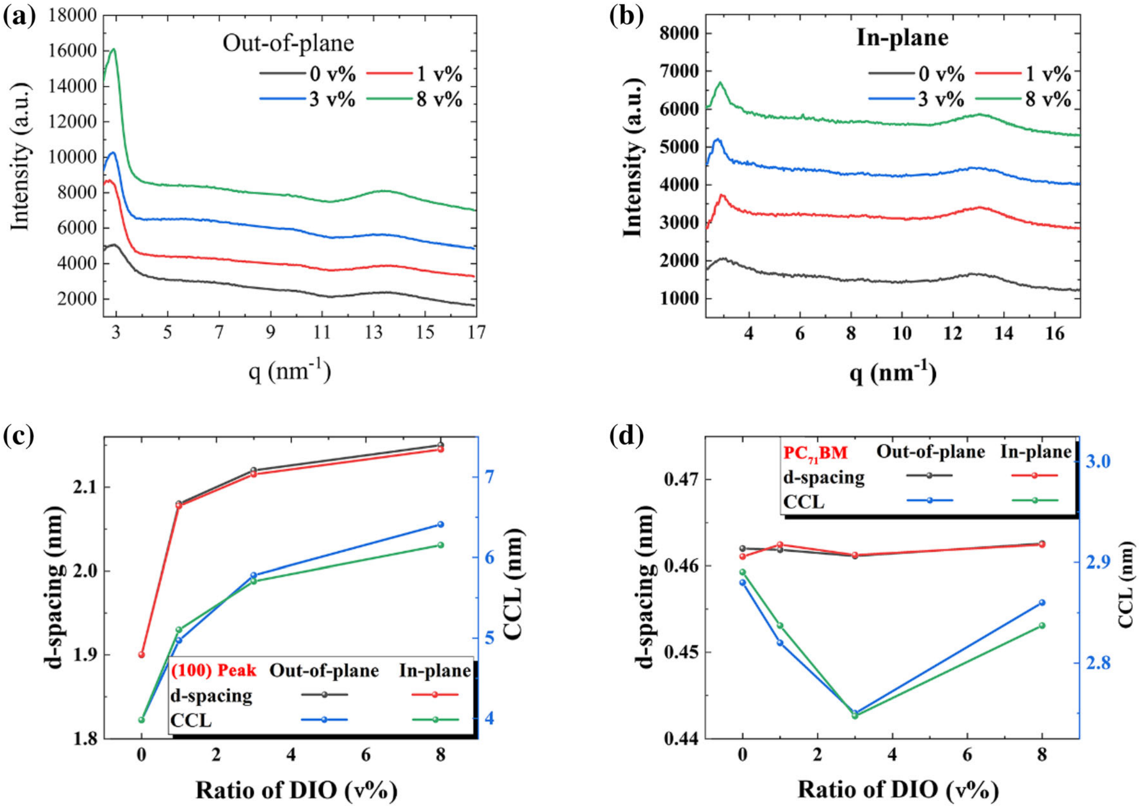

Fig. 5 (Color online) 1D profiles integrated from 2D patterns in the **a** out-of-plane and **b** in-plane directions. Crystal coherence length and *d*-spacing values of **c** (100) peaks and **d** [6,6]-phenyl C_{71}-butyric acid methyl ester rings of blends with various ratios of 1,8-diiodoctane. CCL, crystal coherence length; DIO, 1,8-diiodoctane

Table 2 Crystal coherence length and lattice space values of the (100) peaks and [6,6]-phenyl C_{71}-butyric acid methyl ester rings in the out-of-plane direction for blends with various ratios of 1,8-diiodoctane

Ratio of DIO	(100) peak *d*-spacing (nm)	(100) peak CCL (nm)	$PC_{71}BM$ *d*-spacing (nm)	$PC_{71}BM$ CCL (nm)
0 vol%	1.90	3.98	0.46	2.88
1 vol%	2.08	4.97	0.46	2.82
3 vol%	2.12	5.78	0.46	2.75
8 vol%	2.15	6.41	0.46	2.86

DIO, 1,8-diiodoctane; CCL, crystal coherence length; $PC_{71}BM$, [6,6]-phenyl C_{71}-butyric acid methyl ester; *d*-spacing, lattice space

various ratios of DIO, while the peak position was approximately constant.

The *d*-spacing and CCL values of the (100) peaks are shown in Fig. 5c. The detailed values integrated from the out-of-plane and in-plane directions are summarized in Table 2 and S2, respectively. The CCL values were determined using the Scherre equation, as shown in Eq. (1) [23]:

$$\mathrm{CCL} = \frac{K\gamma}{B\cos\theta}, \tag{1}$$

where B is the FWHM of the peaks, K is a constant with a value of 0.89, γ is the X-ray wavelength, and θ is the Bragg diffraction angle. For the data processing process, the software Fit2D [24] and SG-Tool [25] were used to subtract background scattering and convert 2D patterns into 1D profiles, and the software Peakfit [26] was employed to fit the peak position and FWHM from 1D profiles. The detailed data processing process is shown in the Supporting Information (Sect. 2). The original experimental profiles with background and (100) profiles from Fig. 5a are shown in Fig. S2 and S3, respectively.

As shown in Fig. 5c, the *d*-spacing increased as the proportion of DIO increased, which suggested that the packing distance between the lamellae was enlarged. The CCL also increased with increasing ratio of DIO, indicating that a larger crystal size was obtained when adding more DIO. When the ratio of DIO was 0 vol%, the CCL value of PTB7-Th was approximately 3.98 nm. The values of CCL for blends with various ratios of DIO were significantly larger (5.10, 5.71, and 6.15 nm when adding 1, 3, and 8 vol% DIO, respectively). The values of CCL obtained from the out-of-plane and in-plane directions were approximately the same regardless of the amount of DIO added, indicating that the orientation of the PTB7-Th crystal was not affected by DIO.

The *d*-spacing and CCL values for $PC_{71}BM$ are shown in Fig. 5d. The value of *d*-spacing for $PC_{71}BM$ remained approximately unchanged at 0.46 nm with various ratios of DIO. The CCL value first decreased and then increased as the proportion of DIO increased, where the CCL values were 2.89 nm, 2.84 nm, 2.77 nm, and 2.83 nm. This phenomenon indicated that adding an appropriate proportion of DIO decreases the size of the $PC_{71}BM$ phase, while excessive addition of DIO increases it.

Table 3 GISAXS fitting parameters of blends with 0 and 3 vol% 1,8-diiodoctane

Ratio of DIO	ξ (Å)	D	η (Å)	$2R_{\text{g-PCBM}}$ (Å)	$2R_{\text{g-polymer}}$ (Å)
0 vol%	269	2.97	295	1433	1309
3 vol%	275	2.04	71	251	967

DIO, 1,8-diiodoctane; ξ, domain size where the acceptor is dispersed in polymer; D, fractal dimension of the structure; η, the correlation length of the fractal-like network

To explore the effect of adding DIO on the aggregation of the amorphous phase in the active layer, GISAXS analyses were performed for blends with 0 and 3 vol% DIO to monitor the large-scale morphological information in the active layer. Figure 6a, b show the 2D GISAXS patterns for blends with 0 and 3 vol% DIO. The 1D GISAXS profiles are shown in Fig. 6c, which were integrated from the 2D patterns in the in-plane direction at the value of q_z near the reflected position to obtain enhanced signals. The fitting parameters obtained from GISAXS data were fitted with the Debye–Anderson–Brumberger term [27] in the low q region (0.025–0.5 nm^{-1}) as shown in Table 3. The fitting equation is shown in Eq. (2):

$$I(q) = \frac{A_1}{\left[1 + (q\xi)^2\right]^2} + A_2\langle P(q,R)\rangle S(q,R,\eta,D) + B. \quad (2)$$

In polymer fullerene systems, the first term is used to model the scattering of dispersive $PC_{71}BM$ in the amorphous domain, and the second term represents the contribution of fractal-like aggregations of $PC_{71}BM$, where q is the scattering wave vector, A1 and A2 are independent fitting parameters, and ξ is traditionally used to estimate the size of the domain where the acceptor is dispersed in polymer, which can be easily identified from the "shoulder" occurring in the 1D GISAXS profile. In the second term, $P(q, R)$ is the form factor modeled as spheres, and S (q, R, η, D) is the structure factor of the cluster domain modeled as a fractal-like network expressed in Eq. (3):

$$S(q) = 1 + \frac{\sin[(D-1)\tan^{-1}(q\eta)]}{(qR)^D}\frac{D\Gamma(D-1)}{\left[1+\frac{1}{(q\eta)^2}\right]^{(D-1)/2}}, \quad (3)$$

where R is the mean spherical radius of the primary particles, η is the correlation length of the fractal-like network, D is the fractal dimension of the structure, and η is the correlation length of the fractal-like network. $2R_{\text{g-polymer}}$ and $2R_{\text{g-PCBM}}$ are the Guinier radii employed to approximately characterize the average domain sizes of the

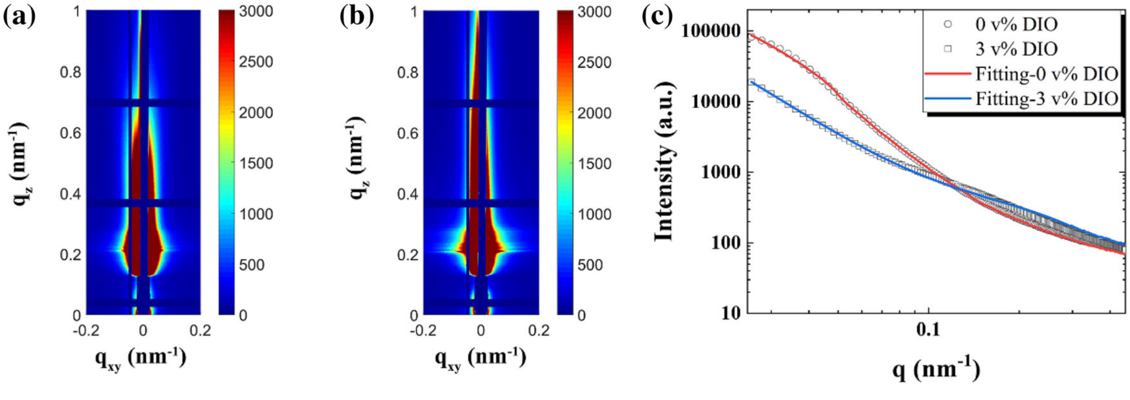

Fig. 6 (Color online) 2D Grazing incidence small angle X-ray scattering patterns for blends with **a** 0 and **b** 3 vol% 1,8-diiodoctane. **c** The 1D profiles integrated from 2D patterns and the fitting curves. DIO, 1,8-diiodoctane

aggregated cluster phases of PTB7-Th and $PC_{71}BM$, which are calculated according to Eqs. (4) and (5):

$$R_{g-\text{polymer}} = \sqrt{\frac{D(D+1)}{2}}\xi, \quad (4)$$

$$R_{g-\text{PCBM}} = \sqrt{\frac{D(D+1)}{2}}\eta. \quad (5)$$

As shown in Table 3, the values of ξ were approximately constant for blends with 0 and 3 vol% DIO, while the CCL values of blends without DIO were apparently smaller than those of blends with 3 vol% DIO, as shown in Fig. 5c. This indicated that the addition of DIO had no effect on the size of the PTB7-Th cluster, but both *d* spacing and crystal size were enhanced with the addition of DIO. The stronger aggregation of $PC_{71}BM$ molecules was obtained in blends without DIO, which was demonstrated by the significantly larger η and $2R_{\text{g-PCBM}}$ values shown in Table 3. However, there were more discrete $PC_{71}BM$ molecules in the active layer with 3 vol% DIO, in which a smaller $2R_{\text{g-polymer}}$ value of the aggregation size of PTB7-Th was obtained (Table 3). Therefore, the addition of DIO weakened the phase separation in the active layer by weakening the aggregation of $PC_{71}BM$ molecules. A homogeneous phase separation scale was obtained, accompanied by smaller clusters of both $PC_{71}BM$ and PTB7-Th. Schematic diagrams of the 3D nanostructures for blends with 0 and 3 vol% DIO were drawn according to the results of GIWAXS and GISAXS measurements, as shown in Fig. 7.

For the blend without DIO shown in Fig. 7a, the CCL value of PTB7-Th was significantly lower than that of blends with 3 vol% DIO, according to the GIWAXS results (Fig. 5c), resulting in poor charge transport efficiency due to the lack of charge transport channels. The larger *D* value (2.97) of the blends without DIO suggested that molecules tended to form spherical clusters, which was also harmful to the charge transport. In addition, the maximum values of CCL and $2R_{\text{g-PCBM}}$ for $PC_{71}BM$ were obtained, indicating that stronger $PC_{71}BM$ aggregation was formed in this case, which resulted in a relatively large phase separation in the active layer. Moreover, a stronger phase separation was also demonstrated by the larger $2R_{\text{g-polymer}}$ value. Thus, exciton dissociation was harmed because of the lack of a donor/acceptor interface caused by the strong phase separation. Owing to these two factors, devices without the addition of DIO showed significantly lower J_{SC} and FF values than devices with added DIO, leading to an apparently lower PCE of 5.49% (Fig. 3). After the addition of DIO (Fig. 7b), the value of CCL for PTB7-Th increased to 5.70 nm. The value of *D* decreased to 2.04, which implied that molecules preferred to form planar aggregations accompanied by a large crystal size, which was beneficial to the improvement of charge transport efficiency, hence, increasing J_{SC} and FF. Simultaneously, the values of CCL for $PC_{71}BM$, $2R_{\text{g-PCBM}}$, and $2R_{\text{g-polymer}}$ decreased with the addition of DIO, implying the formation of weaker phase separation with smaller aggregation clusters, which was also favorable for the enhancement of exciton dissociation and the improvement of J_{SC} and FF by forming more

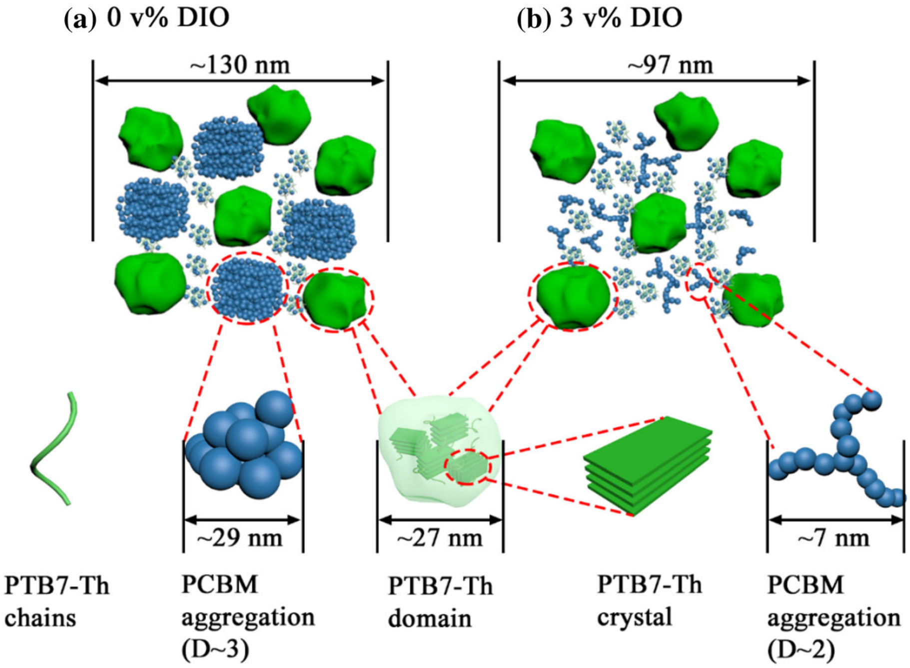

Fig. 7 (Color online). Schematic diagrams of the 3D nanostructures drawn according to the results of grazing incidence wide-angle X-ray scattering and GISAXS measurements for blend films with **a** 0 and **b** 3 vol% 1,8-diiodoctane. DIO, 1,8-diiodoctane; PTB7-Th, poly[(ethylhexyl-thiophenyl)-benzodithiophene-(ethylhexyl)-thienothiophene]; $PC_{71}BM$, 6,6-Phenyl C_{71} butyric acid methyl ester

donor/acceptor interfaces. Therefore, the PCE of the device can be improved (Fig. 3).

3.3 In situ investigation of morphology evolution and correlations with the degradation of thermal stability

In situ GISAXS measurements were performed for PTB7-Th/$PC_{71}BM$ blend films with 0 and 3 vol% DIO to explore the large-scale morphological evolution during the thermal annealing process, as shown in Figs. S4 and S5. No significant change in the 1D curves was observed during thermal annealing of the blend films, regardless of the proportion of DIO added. This indicates that the effect of short-term thermal annealing on the aggregation of amorphous molecules in the active layer was insignificant. The size of the aggregation, size of the fractal network, and fractal dimension were almost unchanged. No large-scale phase separation was induced after thermal annealing, which is consistent with the results in Fig. 4b, where the values of V_{OC} remained approximately constant for devices after thermal annealing, regardless of the addition proportion of DIO. Therefore, the degradation of the device PCE was attributed to the small-scale morphological evolution, which was closely related to the J_{SC} and FF of the devices.

To explore the mechanism of increasing DIO harming device thermal stability, in situ GIWAXS measurements were performed during the thermal annealing process for PTB7-Th/$PC_{71}BM$ blends with various ratios of DIO. To simulate the conventional thermal annealing strategy that directly places devices on a hot plate that has been heated to a specified temperature, an annealing strategy that placed devices on the hot plate at room temperature (25 °C), which was then heated to the annealing temperature (100 °C) at a heating rate of 20 °C/min, was employed. Figure 8 shows the 1D profiles of GIWAXS during the thermal annealing process obtained in the out-of-plane direction for blend films with different ratios of DIO. A similar transition in the (100) peak was observed for all blend films, regardless of the proportion of DIO. Taking the blend film with 3 vol% DIO as an example, as the annealing time increased, the FWHM of the original (100) peak in the out-of-plane direction gradually increased from 0.99 to 1.23 nm^{-1}, and the peak intensity gradually decreased, which led to the gradual disappearance of the original (100) peak. Simultaneously, a newly formed (100) peak occurred at the position with a higher q value ($q = 3.04$ nm^{-1}) accompanied by a gradual decrease in the FWHM to 0.78 nm^{-1}, and peak intensity gradually increased. The detailed values of the peak position and FWHM are summarized in Table S3–S6. This indicates

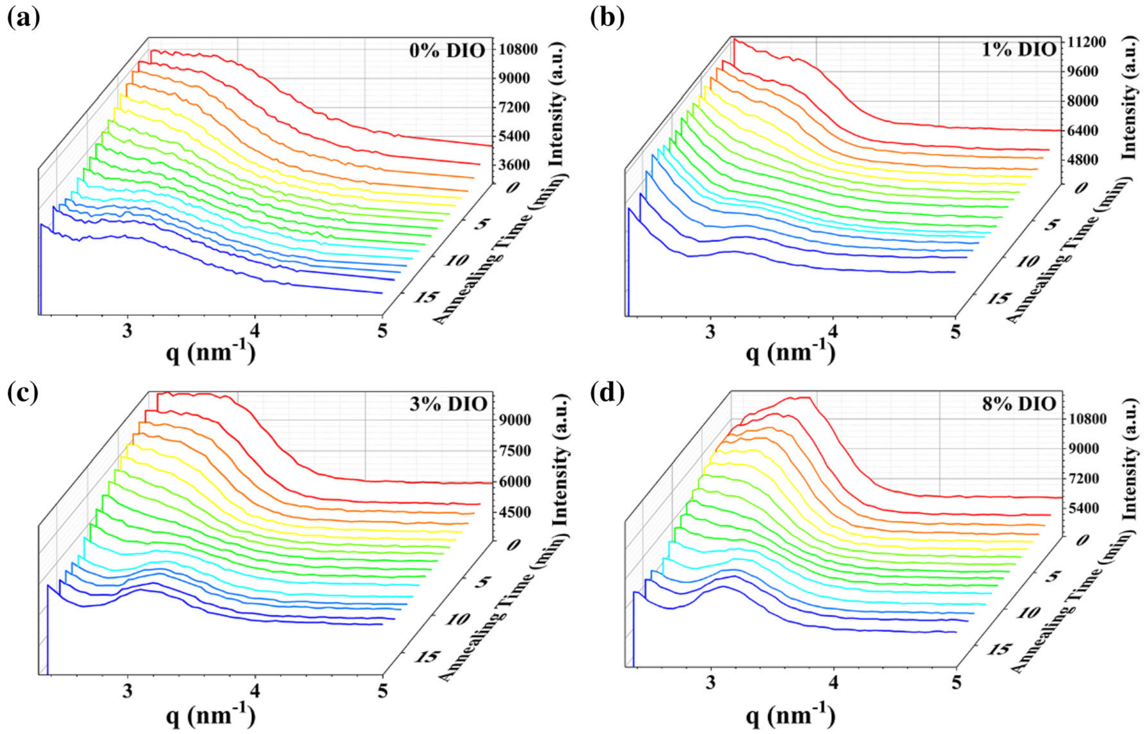

Fig. 8 (Color online) The 1D profiles of grazing incidence wide-angle X-ray scattering obtained in the out-of-plane direction for blend films with **a** 0, **b** 1, **c** 3, and **d** 8 vol% 1,8-diiodoctane during thermal annealing at 100 °C for 10 min, where 0 represents the temperature before annealing (25 °C). DIO, 1,8-diiodoctane

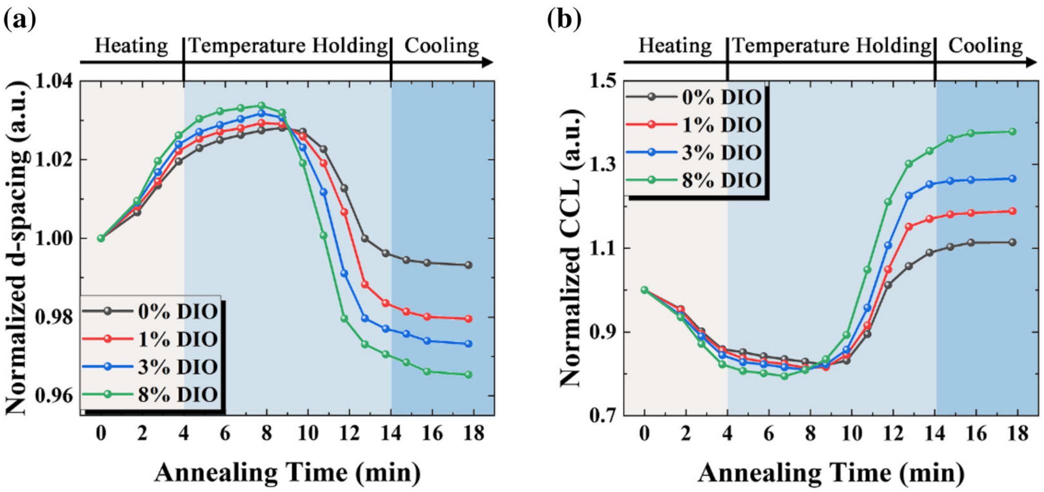

Fig. 9 (Color online) Normalized **a** lattice space and **b** crystal coherence length obtained from the (100) peak in the out-of-plane direction for blends with various ratios of 1,8-diiodoctane during thermal annealing at 100 °C. "0" represents the value obtained at 25 °C. The heating and cooling rate was 20 °C/min. *d*-spacing, lattice space; CCL, crystal coherence length; DIO, 1,8-diiodoctane

Table 4 Values of crystal coherence length and lattice space of (100) peaks integrated from the out-of-plane direction after thermal annealing at 100 °C for 10 min

Ratio of DIO	0 vol%	1 vol%	3 vol%	8 vol%
d-spacing (nm)	1.89	2.04	2.06	2.07
CCL (nm)	4.43	6.07	7.22	8.48

CCL, crystal coherence length; *d*-spacing, lattice space; DIO, 1,8-diiodoctane

that PTB7-Th crystallization could be refactored during the temperature holding process, where the original crystallization was destroyed and new crystallization was formed, accompanied by molecular nucleation and crystal growth processes. It can be concluded from Fig. 8 that the transition of the (100) peak became more drastic as the proportion of DIO increased. In addition, as shown in Table S7–S10, it remained approximately unchanged for both the peak width and peak position of $PC_{71}BM$ during thermal annealing, which implies that the effect of short-term thermal annealing on the $PC_{71}BM$ crystal could be ignored.

The evolution of the normalized *d*-spacing integrated from the out-of-plane (100) peak for blend films with various ratios of DIO during thermal annealing at 100 °C is shown in Fig. 9a. The detailed values of *d*-spacing and CCL after thermal annealing are summarized in Table 4. As shown in Fig. 9a, the same trends occurred, wherein the values of *d*-spacing increased initially and then decreased for all blend films with various ratios of DIO. The difference was that both the increasing and decreasing rates of *d*-space increased as the proportion of DIO increased. The maximum values of *d*-spacing were 102.8%, 102.9%, 103.2%, and 103.4% of their initial values, and the final values were 99.3%, 98.0%, 97.3%, and 96.5% of their initial values for blends with 0, 1, 3, and 8 vol% DIO, respectively. It was indicated that the blend film with more DIO added would suffer more drastic evolution in the *d*-spacing. Moreover, the time at which *d*-spacing started to decrease and CCL started to increase was advanced as the proportion of DIO increased, where the time was approximately 2 min earlier for blends with 8 vol% DIO (about 8 min after thermal annealing started) than for the blends without DIO (approximately 10 min after thermal annealing started), which also suggested that the addition of DIO could facilitate the morphological evolution during the annealing process.

The evolution of the normalized value of CCL integrated from the out-of-plane (100) peak for blend films with various ratios of DIO during thermal annealing at 100 °C is shown in Fig. 9b. The same trends wherein CCL first decreased and then increased were obtained from blend films, regardless of the amount of DIO. Similarly, larger increasing and decreasing rates of CCL were observed as the proportion of DIO increased. The minimum values of CCL were 82.1%, 81.4%, 81.0%, and 79.5%, and the final values were 111.4%, 118.9%, 126.6%, and 137.8% of their initial values for blends with 0, 1, 3, and 8 vol% DIO, respectively. These results indicate that the morphological stability of the blends decreased with an increase in the proportion of DIO, which behaved as a faster morphological evolution by a large margin, as shown in Figs. 8 and 9, resulting in more severe degradation of device thermal stability as more DIO was added (Fig. 3).

In the heating stage, as shown in Fig. 9, the CCL first decreased, which resulted in the reduction of charge transport channels. Simultaneously, a looser packing with a larger *d*-spacing value was formed due to the destruction of the original crystal, which allowed the $PC_{71}BM$ molecules to diffuse into the polymer domains to form more interfaces between the donor and acceptor, thereby enhancing exciton dissociation. In the temperature holding stage, the CCL continued to decrease at a relatively slower rate compared to the decreasing rate in the heating stage. Meanwhile, the *d*-spacing increased at a slower rate. These results demonstrated that the destruction of polymer crystalline phase was still in progress, while the slower evolution slowed the decay rate of charge transport, which may have balanced the effects of weakened charge transport and improved the donor/acceptor interface. Subsequently, as the annealing time increased, the value of CCL increased, accompanied by newly formed charge transport channels, which facilitated the electron mobility and hole mobility in the active layer, thereby enhancing the device PCE and decreasing the recombination loss. However, the interface between the donor and acceptor was weakened owing to the enlarged phase separation due to crystal growth. In the cooling stage, the CCL continued to increase, while the growth rate gradually slowed. However, the final crystal size became too large, resulting in unfavorable phase separation that harmed the photogenerated exciton dissociation, thereby decreasing J_{SC} and FF.

When the devices were thermally annealed, the varying rates of CCL and *d*-spacing in all stages increased as the proportion of DIO increased, which suggested that the addition of DIO causes the active layer to become unstable and facilitate the rate of morphological evolution. The blends with more DIO suffered a more drastic morphological evolution, which was apparently unfavorable for the thermal stability of the device. Therefore, the residual PCE gradually decreased as the proportion of DIO increased (Fig. 4).

3.4 Mechanism of analysis of the effect of DIO on the morphology–performance relationship

Figure 10 shows a schematic diagram of the morphological evolution of blends with 0 and 3 vol% DIO during the thermal annealing processes. DIO is a selective solvent additive that can selectively dissolve $PC_{71}BM$ [28]. In addition, the boiling point of DIO (332 °C) [29] is significantly higher than that of the solvent chlorobenzene (130.9 °C) [30]. As shown in Fig. 10a, when no DIO was added, large-scale sphere $PC_{71}BM$ clusters were formed, leading to a strong phase separation between PTB7-Th and $PC_{71}BM$, which was demonstrated by the larger values of $2R_{g\text{-PCBM}}$ and $2R_{g\text{-polymer}}$ listed in Table 3. When DIO was added (Fig. 10b), part of the clustered $PC_{71}BM$ was dissolved into discrete molecules, and the shape of the cluster became planar, accompanied by decreased values of CCL for $PC_{71}BM$ and $2R_{g\text{-PCBM}}$ (Fig. 5d and Table 3). Discrete $PC_{71}BM$ molecules could diffuse into the polymer-rich

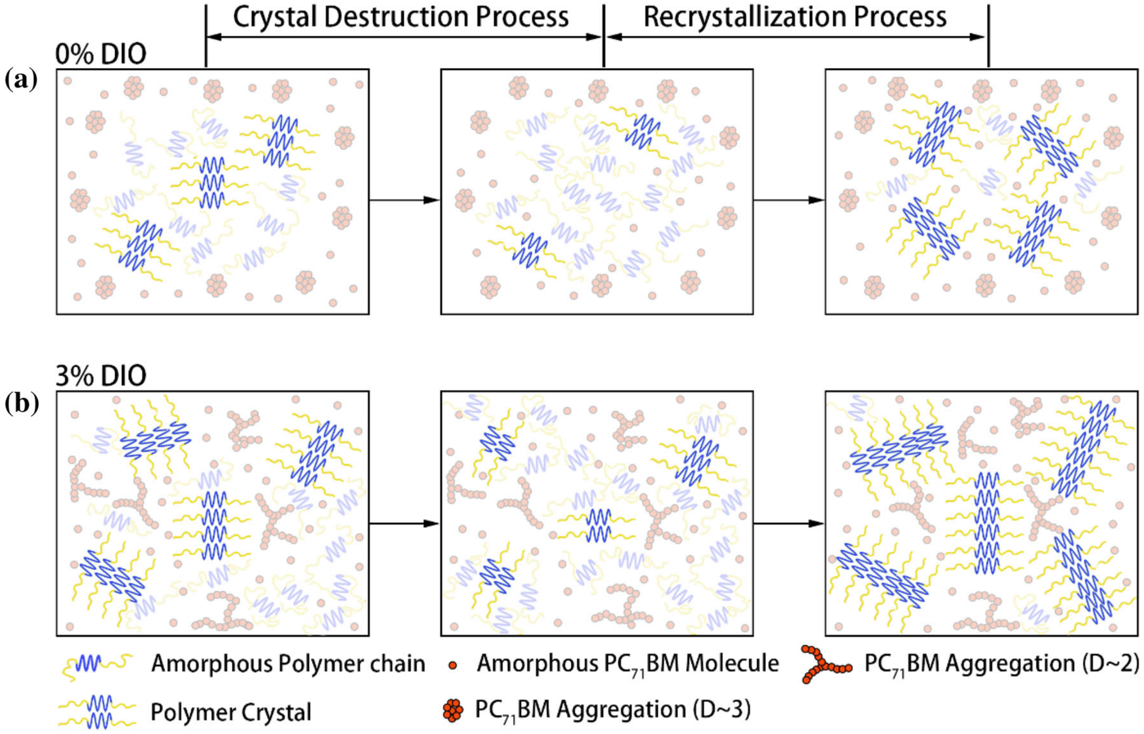

Fig. 10 (Color online) Schematic diagram of the morphological evolution of blends with 0 and 3 vol% 1,8-diiodoctane during thermal annealing. DIO, 1,8-diiodoctane; $PC_{71}BM$, [6,6]-phenyl C_{71}-butyric acid methyl ester

domains and even the crystal domains of PTB7-Th during the film-forming process, owing to the slower volatilization of DIO, leading to an increase in the *d*-spacing of PTB7-Th as the ratio of DIO increased (Fig. 5c). Subsequently, a heterogeneous nucleation and crystal growth process was observed, where the discrete $PC_{71}BM$ molecules had an effect similar to that of the nucleating agent for PTB7-Th. The *d*-spacing, and crystal size of PTB7-Th increased as the proportion of DIO increased (Fig. 5c). When the DIO ratio was increased to 8 vol%, many $PC_{71}BM$ molecules were dissolved in DIO. Owing to the higher boiling point of DIO, chlorobenzene volatilized before DIO during the film-forming process. Afterward, the excessive $PC_{71}BM$ molecules dissolved in DIO formed a new large-scale $PC_{71}BM$ cluster during the volatilization of DIO, leading to an enlarged CCL of $PC_{71}BM$, as shown in Fig. 5d.

For the morphological evolution during thermal annealing, there were two stages; the crystal destruction process and recrystallization process, which corresponded to the CCL decreasing and increasing stages, respectively, as shown in Fig. 9b. Organic photovoltaic molecules have long flexible side chains, allowing molecular chains to relax at temperatures below the glass transition temperature (T_g) [31], which is approximately 125 °C for PTB7-Th [32]. When the annealing process started, the original crystal was destroyed first because of the strong relaxation of the molecules at this temperature. The addition of DIO can decrease the T_g of PTBT-Th [32]; therefore, a stronger molecular relaxation occurred at the annealing temperature for blends with added DIO, which led to a more significant decrease in CCL in the first stage of thermal annealing (Fig. 9). In the second stage, molecular interaction and movement caused amorphous molecules to nucleate and crystallize again to form new crystals with gradually decreased *d*-spacing and increased CCL. For blends with DIO, there were many discrete $PC_{71}BM$ molecules distributed in the polymer domain, which could facilitate the nucleation and crystallization of PTB7-Th (Fig. 10b). Hence, the crystal growth rate and growth starting time both increased as the proportion of DIO increased (Fig. 9). Therefore, more drastic morphological evolutions induced when the proportion of DIO was increased resulted in morphological instability and subsequently, led to a relatively poor thermal stability compared to that of devices without DIO.

4 Conclusion

In this study, the effect of the DIO additive on the PCE and thermal stability of the PTB7-Th/$PC_{71}BM$ device was investigated in depth using an in situ GIWAXS technique that we developed in the beamline BL16B1 at SSRF. The PCE first increased and then decreased as the proportion of DIO increased, achieving the highest value of 9.17% with 3 vol% DIO. In addition, gradual degradation in thermal stability with an increasing DIO proportion occurred, where the residual PCEs after thermal annealing were 90.4%, 77.6%, 75.8%, and 71.4% for devices with 0, 1, 3, and 8 vol% DIO, respectively. GIWAXS and GISAXS measurements showed that the device with 3 vol% DIO could form a favorable active layer morphology with appropriate donor crystal size, aggregation size of amorphous molecules, and phase separation, which offered plenty of donor/acceptor interfaces and charge transport channels to enhance photogenerated exciton dissociation and electron and hole transport. Hence, the optimum PCE was obtained for the device with 3 vol% DIO. However, when the proportion of DIO was 8 vol%, excessive $PC_{71}BM$ was dissolved in DIO, which would form larger aggregates during the film-forming process to harm the device PCE. In situ GIWAXS measurements revealed that the rate of morphological evolution increased as the proportion of DIO increased. The acceptor of $PC_{71}BM$ was partly dissolved by DIO into discrete molecules, which diffused into polymer-rich domains and had an effect similar to that of the PTB7-Th nucleating agent, leading to enhanced crystallization. However, a fast morphological evolution was also induced by the addition of DIO during thermal annealing, thereby resulting in poorer thermal stability. These results also showed the significance, importance, and feasibility of the in situ GIWAXS technique that we developed at BL16B1.

Acknowledgements The authors thank the colleagues at the SAXS beamlines (BL10U1, BL19U2, and BL14B1) of the Shanghai Synchrotron Radiation Facility for their support and discussions.

Author contributions All authors contributed to the study conception and design. Material preparation, data collection and analysis were performed by Da Huang, Chun-Xia Hong, Jian-Hua Han, and Chun-Ming Yang. The first draft of the manuscript was written by Da Huang and all authors commented on previous versions of the manuscript. All authors read and approved the final manuscript.

References

1. Z. Hu, J. Wang, X. Ma et al., A critical review on semitransparent organic solar cells. Nano Energy **78**, 105376 (2020). https://doi.org/10.1016/j.nanoen.2020.105376
2. X. Ma, A. Zeng, J. Gao et al., Approaching 18% efficiency of ternary organic photovoltaics with wide bandgap polymer donor and well compatible Y6: Y6–1O as acceptor. Natl. Sci. Rev. **8**, nwaa305 (2020). https://doi.org/10.1093/nsr/nwaa305
3. X. Wang, Q. Sun, J. Gao et al., Ternary organic photovoltaic cells exhibiting 17.59% efficiency with two compatible Y6 derivations as acceptor. Sol. RRL **5**, 2100007 (2021). https://doi.org/10.1002/solr.202100007

4. Z. Hu, L. Yang, W. Gao et al., Over 15.7% efficiency of ternary organic solar cells by employing two compatible acceptors with similar LUMO levels. Small **16**, e2000441 (2020). https://doi.org/10.1002/smll.202000441
5. S. Guo, W. Wang, E.M. Herzig et al., Solvent–morphology–property relationship of PTB7: PC71BM polymer solar cells. ACS Appl. Mater. Interfaces **9**, 3740–3748 (2017). https://doi.org/10.1021/acsami.6b14926
6. Z. Yi, W. Ni, Q. Zhang et al., Effect of thermal annealing on active layer morphology and performance for small molecule bulk heterojunction organic solar cells. J. Mater. Chem. C **2**, 7247–7255 (2014). https://doi.org/10.1039/c4tc00994k
7. D. Zomerman, J. Kong, S.M. McAfee et al., Control and characterization of organic solar cell morphology through variable-pressure solvent vapor annealing. ACS Appl. Energy Mater. **1**, 5663–5674 (2018). https://doi.org/10.1021/acsaem.8b01214
8. Q. An, X. Ma, J. Gao et al., Solvent additive-free ternary polymer solar cells with 16.27% efficiency. Sci. Bull. **64**, 504–506 (2019). https://doi.org/10.1016/j.scib.2019.03.024
9. C. McDowell, M. Abdelsamie, M.F. Toney et al., Solvent additives: key morphology-directing agents for solution-processed organic solar cells. Adv. Mater. **30**, e1707114 (2018). https://doi.org/10.1002/adma.201707114
10. C.M. Benavides, S. Rechberger, E. Spiecker et al., Improving spray coated organic photodetectors performance by using 1,8-diiodooctane as processing additive. Org. Electron. **54**, 21–26 (2018). https://doi.org/10.1016/j.orgel.2017.12.022
11. A.J. Pearson, P.E. Hopkinson, E. Couderc et al., Critical light instability in CB/DIO processed PBDTTT-EFT: PC71BM organic photovoltaic devices. Org. Electron. **30**, 225–236 (2016). https://doi.org/10.1016/j.orgel.2015.12.024
12. P. Muller-Buschbaum, The active layer morphology of organic solar cells probed with grazing incidence scattering techniques. Adv. Mater. **26**, 7692–7709 (2014). https://doi.org/10.1002/adma.201304187
13. R. Szostak, S. Sanchez, P.E. Marchezi et al., Revealing the perovskite film formation using the gas quenching method by in situ GIWAXS: morphology, properties, and device performance. Adv. Funct. Mater. **31**, 2007473 (2020). https://doi.org/10.1002/adfm.202007473
14. C. Xu, H. Chen, Z. Zhao et al., 14.46% Efficiency small molecule organic photovoltaics enabled by the well trade-off between phase separation and photon harvesting. J. Energy Chem. **57**, 610–617 (2021). https://doi.org/10.1016/j.jechem.2020.09.025
15. H. Xu, Z. Zhao, Current status and progresses of SSRF project. Nucl. Sci. Tech. **19**, 1–6 (2008). https://doi.org/10.1016/S1001-8042(08)60013-5
16. F. Tian, X. Li, Y. Wang et al., Small angle X-ray scattering beamline at SSRF. Nucl. Sci. Tech. **26**, 030101 (2015). https://doi.org/10.13538/j.1001-8042/nst.26.030101
17. W. Kim, J.K. Kim, E. Kim et al., Conflicted effects of a solvent additive on PTB7: PC71BM bulk heterojunction solar cells. J. Phys. Chem. C **119**, 5954–5961 (2015). https://doi.org/10.1021/jp510996w
18. N.K. Elumalai, A. Uddin, Open circuit voltage of organic solar cells: an in-depth review. Energy Environ. Sci. **9**, 391–410 (2016). https://doi.org/10.1039/C5EE02871J
19. B.C. Thompson, J.M. Frechet, Polymer-fullerene composite solar cells. Angew. Chem. Int. Ed. Engl. **47**, 58–77 (2008). https://doi.org/10.1002/anie.200702506
20. L.K. Jagadamma, M.T. Sajjad, V. Savikhin et al., Correlating photovoltaic properties of a PTB7-Th:PC71BM blend to photophysics and microstructure as a function of thermal annealing. J. Mater. Chem. A **5**, 14646–14657 (2017). https://doi.org/10.1039/c7ta03144k
21. S.B. Dkhil, M. Pfannmöller, M.I. Saba et al., Toward high-temperature stability of PTB7-based bulk heterojunction solar cells: impact of fullerene size and solvent additive. Adv. Energy Mater. **7**, 1601486 (2017). https://doi.org/10.1002/aenm.201601486
22. Q. Wan, X. Guo, Z. Wang et al., 10.8% efficiency polymer solar cells based on PTB7-Th and PC71BM via binary solvent additives treatment. Adv. Funct. Mater. **26**, 6635–6640 (2016). https://doi.org/10.1002/adfm.201602181
23. A. Patterson, The Scherrer formula for X-ray particle size determination. Phys. Rev. **56**, 978 (1939). https://doi.org/10.1103/PhysRev.56.978
24. A.P. Hammersley, FIT2D: a multi-purpose data reduction, analysis and visualization program. J. Appl. Crystallogr. **49**, 646–652 (2016). https://doi.org/10.1107/S1600576716000455
25. N. Zhao, C. Yang, F. Bian. SGTools: data processing and analysis for X-ray scattering. http://www.sgtools.cc/
26. S. S. Inc., Tools for science. https://systatsoftware.com/
27. H.C. Liao, C.S. Tsao, T.H. Lin et al., Quantitative nanoorganized structural evolution for a high efficiency bulk heterojunction polymer solar cell. J. Am. Chem. Soc. **133**, 13064–13073 (2011). https://doi.org/10.1021/ja202977r
28. L. Zhao, S. Zhao, Z. Xu et al., Two effects of 1, 8-diiodooctane on PTB7-Th: PC71BM polymer solar cells. Org. Electron. **34**, 188–192 (2016). https://doi.org/10.1016/j.orgel.2016.04.014
29. S. Holliday, C.K. Luscombe, Low boiling point solvent additives for improved photooxidative stability in organic photovoltaics. Adv. Electron. Mater. **4**, 1700416 (2018). https://doi.org/10.1002/aelm.201700416
30. Y. Li, Y. Guo, T. Zhu et al., Adsorption and desorption of SO2, NO and chlorobenzene on activated carbon. J. Environ. Sci. **43**, 128–135 (2016). https://doi.org/10.1016/j.jes.2015.08.022
31. C. Yang, I. Takahashi, Unusual thickness relaxation of spin-coated polystyrene ultrathin films in the glassy state. Polymer **186**, 121972 (2020). https://doi.org/10.1016/j.polymer.2019.121972
32. K.S. Wienhold, V. Körstgens, S. Grott et al., Effect of solvent additives on the morphology and device performance of printed nonfullerene acceptor based organic solar cells. ACS Appl. Mater. Interfaces **11**, 42313–42321 (2019). https://doi.org/10.1021/acsami.9b16784